GEOPHYSICS, VOL. 70, NO. 5 (SEPTEMBER-OCTOBER 2005); P. U51–U65, 21 FIGS., 1 TABLE.
10.1190/1.2049350

Depth-consistent reflection tomography using PP and PS seismic data

Stig-Kyrre Foss[1], Bjørn Ursin[2], and Maarten V. de Hoop[3]

ABSTRACT

We present a method of reflection tomography for anisotropic elastic parameters from PP and PS reflection seismic data. The method is based upon the differential semblance misfit functional in scattering angle and azimuth (DSA) acting on common-image-point gathers (CIGs) to find fitting velocity models. The CIGs are amplitude corrected using a generalized Radon transform applied to the data. Depth consistency between the PP and PS images is enforced by penalizing any mistie between imaged key reflectors. The mis-tie is evaluated by means of map migration-demigration applied to the geometric information (times and slopes) contained in the data. In our implementation, we simplify the codepthing approach to zero-scattering-angle data only. The resulting measure is incorporated as a regularization in the DSA misfit functional. We then resort to an optimization procedure, restricting ourselves to transversely isotropic (TI) velocity models. In principle, depending on the available surface-offset range and orientation of reflectors in the subsurface, by combining the DSA with codepthing, the anisotropic parameters for TI models can be determined, provided the orientation of the symmetry axis is known. A proposed strategy is applied to an ocean-bottom-seismic field data set from the North Sea.

INTRODUCTION

We demonstrate the use of annihilator-based migration velocity analysis (MVA), related to the differential semblance (Symes and Carazzone, 1991) approach, on joint PP and PS reflection seismic data. The MVA is carried out here by analyzing the waveform residual moveout and amplitude variations in common-image-point gathers (CIGs) parameterized by scattering angle and azimuth. Annihilators on such gathers simplify to differentiation in angle, leading to the differential semblance in angle (DSA) functional introduced in Brandsberg-Dahl et al. (2003b). The misfit function associated with the annihilator approach is unique in that it depends smoothly on the velocity model. As is common in MVA, we model the reflection data in the single scattering approximation, yielding a forward-scattering operator that, given a velocity model, maps reflectors to reflections. By a gradient-based search of the model space, the range of the forward-scattering operator is adapted to contain the data. Data are in the range if they can be predicted by the operator. Thus, the goal is to obtain an elastic velocity model from PP and PS reflection seismic data combined; we restrict ourselves to transversely isotropic (TI) media with a given symmetry axis.

Annihilators detect whether the data are in the range of the forward-scattering operator (Stolk and de Hoop, 2002). They have their counterpart in the image domain. The data are in the range if the CIGs obtained from the data — parameterized by (subsurface) scattering angle and azimuth between incoming and scattered rays at the image point — are uniform, i.e., they are flat and show angle-independent amplitude; annihilators emerge as derivatives with angle.

Because MVA typically is based on a small collection of reflections, one expects an inherent nonuniqueness in the inverse problem of determining the velocity model. We consider a velocity model to be acceptable if the reflections are in the range of the forward-scattering operator. In this paper, we search in the class of acceptable velocity models for a model that not only predicts the PP and PS reflections in time but also ties the PP and PS images of corresponding reflectors in depth. In this so-called codepthing process, one needs to ensure that the PP and PS images indeed have these reflectors in common, which requires a degree of seismic interpretation. Codepthing can also be carried out with well data.

Traditionally, MVA exploits the redundancy in the data by studying the residual moveout on CIGs (Al-Yahya, 1989). Flat gathers guarantee a velocity model resulting in a well-focused

Manuscript received by the Editor April 14, 2004; revised manuscript received February 10, 2005; published online September 12, 2005.
[1]Formerly Norwegian University of Science and Technology, Department of Mathematical Sciences, Trondheim, Norway. Presently Statoil Research, Arkitekt Ebbells vei 10, 2005 Trondheim, Norway. E-mail: skyf@statoil.com.
[2]Norwegian University of Science and Technology, Department of Petroleum Engineering and Applied Geophysics, NO-7491 Trondheim, Norway. E-mail: bjornu@ipt.ntnu.no.
[3]Colorado School of Mines, Center for Wave Phenomena, 1500 Illinois Street, Golden, Colorado 80401-1887. E-mail: mdehoop@dix.mines.edu.

(sharp) image. Image gathers are formed from data subsets, typically parameterized by offset. The differential semblance misfit function (Symes and Carazzone, 1991) measures the residual moveout on these CIGs and quantifies the degree of fit between traces by a local derivative in offset. This procedure has been carried out by Plessix et al. (2000) and Chauris and Noble (2001), among others.

In the presence of caustics, an image generated from common-offset data will contain artifacts (false reflectors). To remedy this in the MVA, the derivative with respect to offset in differential semblance is replaced by the above-mentioned annihilators of the data. Here, we follow a simplification based on replacing the derivative with respect to (surface) offset with derivatives with respect to (subsurface) scattering angle and azimuth. This simplification introduces a risk — namely, in the presence of caustics, an image gather will contain false reflectors.

In the absence of caustics, the differential semblance measure seems to yield a global minimizer (Symes, 2000). This means that the initial velocity model can be quite far from an acceptable model, and optimization will still result in an acceptable model in the sense explained above. We ensure that the amplitude versus scattering angle and azimuth (AVA) behavior on the CIGs — associated with a reflection coefficient or contrast-source radiation patterns — does not contribute to the differential semblance in angle.

Several authors approach the problem of joint PP and PS velocity analysis (Sollid and Ettrich, 1999; Berthet et al., 2001; Stopin and Ehinger, 2001; Alerini et al., 2002; Grechka and Tsvankin, 2002b; Broto et al., 2003; Sollid and Ursin, 2003); see Herrenschmidt et al. (2001) for a review. The diodic nature of PS reflections (Thomsen, 1999) demands a treatment of MVA different from that for PP reflections. The diodic nature is a consequence of the fact that PS reflections are nonreciprocal in source and receiver; indeed, the reciprocal of PS is SP. It is also a well-known difficulty that images of a common geological reflector from PP and PS reflections often do not match in depth. There are several reasons for this. The velocity-depth ambiguity (Stork and Clayton, 1986; Bube, 1995) is intimately connected to ray coverage and acquisition aperture. In addition, anisotropy must be included to compute depth-consistent PP and PS images because an isotropic assumption can cause severe depth errors in the presence of anisotropy. And then, with an anisotropic medium there is added ambiguity in the interplay between the different elastic parameters (Bube and Meadows, 1999). Versteeg (1993) shows how continuously smoothing a correct model would recreate the image geometrically yet blur it. One can view these apparent ambiguities as structures in the manifold of acceptable velocity models, i.e., velocity models that recreate the data. The range of the forward-scattering operator does not change significantly between models in this manifold. Tying PP and PS images of common reflectors constrains the manifold of acceptable velocity models.

The PP reflection tomography by means of DSA optimization (Brandsberg-Dahl et al., 2003b) is extended here to PS reflections, accounting for their diodic nature. The key contribution of this paper is a methodology of codepthing the PP and PS CIGs in angle in the framework of angle tomography. In practice, we focus on tying PP and PS images in depth on prior chosen key reflectors that are presumed to be the same based on geologic grounds.

To tie the PP and PS reflections in depth, we use time horizons obtained from paired and picked events in depth on PP and PS images that are map-demigrated to time. Using map migration (Kleyn, 1977; Gjoystdal and Ursin, 1981) of the time horizons for every suggested velocity model, we are able to quantify the depth mismatch automatically. Notice that the time horizons need only be picked once. For the converted-wave events, the ability to perform PS map migration is highly dependent on how close we are to the true model initially; hence, we opt for adapting the PP + PS = SS approach of Grechka and Tsvankin (2002b) to convert PS to SS traveltimes. In this paper we use a zero-offset restriction by map-demigrating normal-incidence-point (NIP) rays (Hubral and Krey, 1980) as suggested by Whitcombe (1994). For the mode-converted waves we use a simplified version of the PP + PS = SS approach using NIP rays to compute approximate zero-offset SS traveltime data.

The outline of the paper is as follows. In the following section, we briefly review PP reflection tomography (Brandsberg-Dahl et al., 2003b) and its extension to mode-converted waves. In the next section, we introduce our codepthing methodology in the framework of DSA optimization by adding a penalizing term to the misfit function. Then we present a stepwise strategy to obtain parameter values of a TI medium with a known symmetry axis. Although the strategy is presented for a 3D medium, we disregard the presence of azimuthal anisotropy. It can be parameterized by v_{P0}, v_{S0}, ε, and δ, which are the vertical P- and S-wave velocities and the Thomsen (1986) parameters, respectively. In Appendix A we summarize our migration to uniform CIGs in scattering angle and azimuth. The formulation here is in three dimensions; the 2.5D formulation and its subtleties, which we use in the field-data case study, are presented in Foss et al. (2005).

Several authors have discussed the point that to obtain information on the δ parameter from reflection moveout analysis, one needs either information of the true depths of a set of reflectors through well logs or large-offset and wide-azimuth PP and PS data in three dimensions in the presence of reflectors with a range of dips (Audebert et al., 2001; Grechka et al., 2002). In the absence of such information, several approaches have been suggested (Alkhalifah and Tsvankin, 1995; Grechka and Tsvankin, 2002b). Here, we first make the choice of setting δ equal to zero considering a quasi-TI medium with a vertical symmetry axis (quasi-VTI). The remaining ε parameter is not the true anisotropy parameter but is an effective one. Second, we design a layer-stripping approach to try and resolve ε and δ separately. Motivated by numerical experiments carried out by Plessix et al. (2000), suggesting the use of differential semblance optimization until a certain rate of improvement is achieved and then switching to semblance optimization (Taner and Koehler, 1969), we investigate the use of differential semblance and semblance combined in a procedure scanning for ε and δ. Finally, we use this methodology on a North Sea ocean-bottom-seismic field data set to obtain (1) a quasi-VTI velocity model and then (2) all parameters of a VTI velocity model.

DIFFERENTIAL SEMBLANCE IN ANGLE

CIGs in scattering angle θ and azimuth ψ are generated with the aid of the generalized Radon transform (GRT) inversion, summarized in Appendix A, of seismic reflection data for a given or current velocity model. Image points in the subsurface are denoted by $\mathbf{y} = (y_1, y_2, y_3)$. Differential semblance is then applied by differentiating with respect to scattering angle and azimuth to these gathers. The outcome of this vanishes if the velocity model used in single-scattering modeling by the GRT predicts the data. Reflection tomography is performed to estimate the parameters describing the smooth part of the medium by kinematic and dynamic ray tracing to compute the different quantities and factors necessary to generate the CIGs.

Each of the parameters describing the velocity model is given a representation with a finite number of coefficients defining a finite-dimensional subspace of models. If we assume that n coefficients, denoted by $\mathbf{m} = (m_1, \ldots, m_n)$, are sufficient to describe fully the smooth part of the medium and that the CIGs generated by equation A-12 are denoted by $\mathcal{I}$ ($\mathbf{y}$, $\mathbf{m}$; θ, ψ), then the DSA misfit function for PP reflections is given by

$$\mathcal{E}_{PP}(\mathbf{m}) = \frac{1}{2}\iiint |\partial_{\theta,\psi}\mathcal{I}_{PP}(\mathbf{y}, \mathbf{m}; \theta, \psi)|^2 \, d\theta \, d\psi \, d\mathbf{y}. \quad (1)$$

A minimum of this functional is found for uniform gathers; uniform gathers guarantee optimal focusing of the structural image.

Because of the diodic nature (Thomsen, 1999) of PS reflections, we split the CIGs contributing to the misfit function into positive and negative constituents, denoted by $\mathcal{I}^+_{PS}$ and $\mathcal{I}^-_{PS}$. In the absence of caustics, the positive constituents are formed from positive acquisition offset data, whereas the negative constituents are formed from negative acquisition offset data. The $\mathcal{I}^{\pm}_{PS}$ CIGs are generated from seismic events where the source and receiver rays intersect at the image point with orientations shown in Figure 1. The splitting is necessary in a tomographic procedure because the rays for the two constituents travel in different parts of the velocity model. The PS misfit function is then given by

$$\mathcal{E}_{PS}(\mathbf{m}) = \frac{1}{2}\iiint \left\{ \left|\partial_{\theta,\psi}\mathcal{I}^+_{PS}(\mathbf{y}, \mathbf{m}; \theta, \psi)\right|^2 + \left|\partial_{\theta,\psi}\mathcal{I}^-_{PS}(\mathbf{y}, \mathbf{m}; \theta, \psi)\right|^2 \right\} d\theta \, d\psi \, d\mathbf{y}. \quad (2)$$

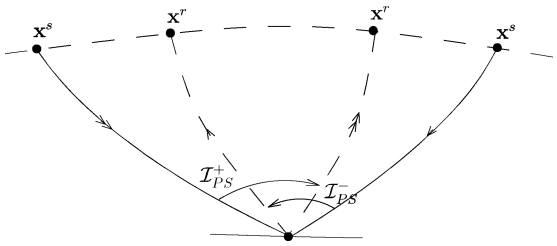

Figure 1. Positive and negative PS CIGs, $\mathcal{I}^+_{PS}$ and $\mathcal{I}^-_{PS}$. The single and double arrows indicate the ray directions in the respective reflection events. The solid and dashed curves are the P- and S-wave legs, respectively.

CODEPTHING PP AND PS IMAGES

Since the GRT approach is based upon a high-frequency approximation and decouples S- from P-wave propagation, we need to consider possible inconsistency in depth of reflectors common in PP and PS images. In reflection tomography, we therefore incorporate a term in the misfit function that penalizes mismatch in depth of a small collection of key reflectors. A key reflector in the structural images is chosen on the basis of coherency and focusing. Finding the key reflectors requires a degree of seismic interpretation where the difficulty is ensuring that the PP and PS imaged reflectors pertain to the same geologic interface.

Let the jth pair of interpreted key reflectors on depth-migrated PP and PS images be given by the graphs of functions z^j_{PP} and z^j_{PS}, $\{[y_1, y_2, z^j_{PP}(y_1, y_2; \mathbf{m})], [y_1, y_2, z^j_{PS}(y_1, y_2; \mathbf{m})]\}$, for a given velocity model $\mathbf{m}$. We refer to the resulting set as the set of reflector graphs. Matching the interfaces in depth can be performed by velocity-model updating, each time carrying out the migration on PP and PS data and performing the interpretation. The key reflectors on the PP and PS images can also be matched to their depths $\{z^j_w(y'_1, y'_2)\}$ derived from well logs at well locations (y'_1, y'_2).

To include the codepthing in our MVA procedure without performing full (GRT) migrations repeatedly, we suggest following a map migration approach instead. The (small) set of picked key reflectors (graphs), yielding position of and normal to each reflector from migrated images, are map-demigrated into PP and PS reflection-time surfaces and slopes (Kleyn, 1977). This information is then considered as data.

For variable velocity models, we subject the reflection-time surfaces and slopes to map migration, reconstructing the key interfaces in depth and thus enabling a geometric comparison. As an approximation here, we restrict the above-mentioned matching procedure to zero scattering angle, i.e., exploding-reflector model data; then only NIP rays to the surface (Hubral and Krey, 1980) are accounted for. Special consideration is needed for the converted-wave case with its diodic behavior.

Pure-mode events

Map demigration

Indicated in Figure 2 are two NIP rays for the reflector point $\mathbf{y}$ for two different wave modes, P-waves and S-waves. The

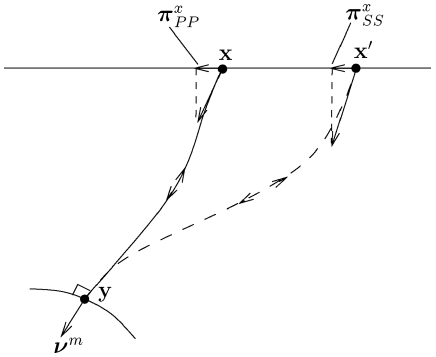

Figure 2. Two normal-incidence-point (NIP) rays for the P- and S-waves from the subsurface point $\mathbf{y}$.

NIP ray for the PP reflection connects **x** and **y**; for the SS reflection, it connects **x**′ and **y**. The two-way NIP ray traveltimes are $\tau_{PP}(\mathbf{x})$ and $\tau_{SS}(\mathbf{x}')$, respectively. Even though the rays of the two wave modes both take off normal to the interface, they usually follow different paths to the surface, as indicated. The PP and SS NIP rays coincide only when the v_P/v_S ratio is constant throughout the velocity model.

Map migration

Using map migration in a given background medium **m**, we map the time horizons and slopes to depth horizons and dips. A particular imaged reflector point is written as $\{y_1, y_2, z^j[y_1, y_2; \mathbf{x}, \tau^j(\mathbf{x}), \boldsymbol{\pi}^{x;j}(\mathbf{x}), \mathbf{m}]\}$, where $\boldsymbol{\pi}^x$ denotes slopes of pure-mode zero-offset data, i.e., the projections of the slowness vectors associated with the NIP rays onto the acquisition surface (see Figure 3). Indicated in Figure 3 is the imaged key reflector point given a different model **m**′. The arrow indicates the movement of image points and dips along the velocity ray. In principle, the process of repeated map migrations does not require that the images of a key reflector be picked again after each velocity-model update.

Converted-mode events

We use a zero-offset version of the PP + PS = SS approach of Grechka and Tsvankin (2002b). The amplitude of a PS event at zero scattering angle vanishes. Nevertheless, in the PS angle gathers we can extrapolate the singular supports to zero angle. In an acceptable velocity model for the PS event, the NIP-P ray connects **y** to **x** and the NIP-S ray connects **y** to **x**′ as in Figure 2. The two-way traveltime is then given by

$$\tau_{PS}(\mathbf{x}, \mathbf{x}') = \frac{\tau_{PP}(\mathbf{x})}{2} + \frac{\tau_{SS}(\mathbf{x}')}{2}, \tag{3}$$

with reflection point **y**. Notice the use of two arguments in the traveltime function for converted modes as there are two emerging points at the acquisition surface; zero scattering angle does not necessarily imply zero offset.

In an unacceptable velocity model, let us assume that we have successfully identified an interface on both a PP image and a PS image that is geologically the same but is imaged at different depths. This situation is sketched in Figure 4, where both the PP and PS images of the key reflector are indicated. In the unacceptable model, the PS event is imaged at **y**′ and the PP event is imaged at **y**, assuming the same **x** position for the NIP-P ray through map demigration; the PS event tied to the PS image has two-way traveltime $\tau_{PS}(\mathbf{x}, \mathbf{x}'')$ ($\mathbf{x}' \neq \mathbf{x}''$ as the model is unacceptable). The zero-scattering-angle PP and PS two-way traveltimes are data obtained from map demigration and are considered to be correct. If we assume that $\mathbf{x}'' \approx \mathbf{x}'$, we can use equation 3 to compute $\tau_{SS}(\mathbf{x}'')$:

$$\tau_{SS}(\mathbf{x}'') \approx 2\tau_{PS}(\mathbf{x}, \mathbf{x}'') - \tau_{PP}(\mathbf{x}). \tag{4}$$

We have obtained pure S-wave NIP two-way traveltimes that we will exploit as data from now on. The techniques of the previous section apply to these data (see Figure 3).

Misfit function for codepthing

The initial interpretations in the set of reflector graphs yield $[\mathbf{x}, \tau^j_{PP}(\mathbf{x}), \boldsymbol{\pi}^{x;j}_{PP}(\mathbf{x})]$ and $[\mathbf{x}, \tau^j_{SS}(\mathbf{x}), \boldsymbol{\pi}^{x;j}_{SS}(\mathbf{x})]$ by map demigration and the PP + PS = SS approximation, equation 4. We are then able to compute the imaged depths of the key reflectors, $[y_1, y_2, z^j_{PP}(y_1, y_2; \tau^j_{PP}, \boldsymbol{\pi}^{x;j}_{PP}, \mathbf{m})]$ and $(y_1, y_2, z^j_{SS}[(y_1, y_2; \tau^j_{SS}, \boldsymbol{\pi}^{x;j}_{SS}, \mathbf{m})]$, automatically through map migration based on the medium parameters **m** governing the P-wave and the S-wave propagation in a discriminate fashion. For example, we can define a misfit function for codepthing, penalizing the mis-tie between the picked PP reflector in depth and the map-migrated SS reflector based on the medium parameters — $\mathbf{m}_S$, say — governing the S-wave propagation, namely,

$$\mathcal{E}_D(\mathbf{m}_S) = \frac{1}{2}\sum_j \iint \left| z^j_{SS}(y_1, y_2; \tau^j_{SS}, \boldsymbol{\pi}^{x;j}_{SS}, \mathbf{m}_S) - z^j_{PP}(y_1, y_2) \right|^2 dy_1 dy_2. \tag{5}$$

The reason to use the depths of interfaces picked on PP images as a reference is that they are usually much better determined in view of the PP versus PS ray coverage. Poorer ray coverage implies an increased ambiguity in reflector depth (Bube, 1995). The misfit function can also be formulated to penalize

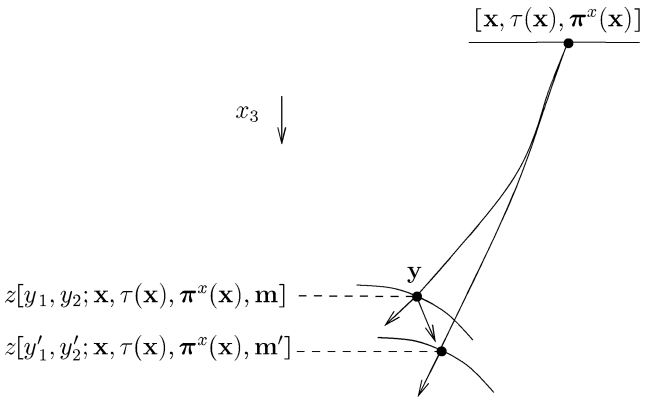

Figure 3. Mapping of the NIP reflection traveltime function and slopes to reflector depths and dips, given a velocity model **m** and **m**′.

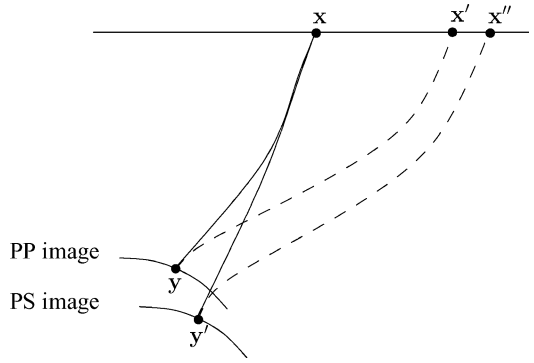

Figure 4. The reflector point imaged at **y** and **y**′ from PP and PS reflection data, respectively, resulting from an inconsistent background model. Indicated are NIP rays from the two reflector points to the acquisition surface. Broken lines are S-wave rays; solid lines indicate P-wave rays.

the mis-tie between PP and SS interfaces and well-log markers $[y_1, y_2, z_w^j(y_1, y_2)]$ at discrete (y_1, y_2) points.

We arrive at a joint reflection tomography and codepthing misfit function,

$$\mathcal{E}(\mathbf{m}) = \lambda_1 \mathcal{E}_{PP}(\mathbf{m}) + \lambda_2 \mathcal{E}_{PS}(\mathbf{m}) + \mu \mathcal{E}_D(\mathbf{m}), \qquad (6)$$

where λ_1, λ_2, and μ are regularization parameters governing the trade-off between uniform CIGs and depth consistency. By setting $\mu = 0$, the search aims at matching the range of the PP and PS forward-scattering operators to the relevant data constituents. The codepthing is accomplished by setting $\mu \gg \lambda_1, \lambda_2 > 0$ and aims at a search in model space without changing the range of the forward-scattering operators. The joint optimization for DSA and codepthing is discussed in Appendix A. The misfit function can be minimized by a gradient-based search of the model space, such as a quasi-Newton method. Motivated by a study of Symes (2000), we conjecture that the minimum of our misfit functions can be obtained by optimization.

STRATEGY FOR DEPTH-CONSISTENT PP AND PS REFLECTION TOMOGRAPHY IN A TI MEDIUM

The strategy for elastic reflection tomography we develop in this section, similar to Sollid and Ettrich (1999), applies particularly in the absence of well data. We consider a TI medium with a known global direction of the symmetry axis. For qP-qSV waves, the medium is described by four parameters: the P- and S-wave velocities v_{P0} and v_{S0} and Thomsen's (1986) δ and ε, defined with respect to the symmetry axis. We approach the problem of estimating the model parameters by using the following steps, reflecting a hierarchy of model complexity (the misfit function is given in equation 6).

1) We carry out isotropic P-wave velocity analysis on PP CIGs using differential semblance in angle ($\lambda_1 = 1, \lambda_2 = 0, \mu = 0$).
2) Keeping the P-wave velocity model obtained in step 1 fixed, we carry out isotropic S-wave velocity analysis on PS CIGs using differential semblance in angle ($\lambda_1 = 0, \lambda_2 = 1, \mu = 0$).
3) We carry out seismic interpretation of the PP and PS images for key reflectors and pick them (including the dips). The reflector picked on the PP (depth) image will yield the reference in the misfit function $\mathcal{E}_D$. We map-demigrate the results, making use of the P- and S-wave velocity models obtained in steps 1 and 2 and derive SS zero-offset time horizons and slopes, which play the role of data for codepthing.
4) We carry out codepthing, keeping the P-wave velocity model from step 1 fixed and updating the S-wave velocity model, map-migrating the data obtained in step 3. The differential semblance in angle contribution to the misfit function plays the role of regularization ($\lambda_1 = 0, \mu \gg \lambda_2 > 0$).
5) We carry out differential semblance in angle optimization of PS CIGs, allowing the model to become anisotropic (TI) by estimating ε with $\delta = 0$ and keeping the P-wave velocity model obtained in step 1 and the ratio of P-wave and S-wave velocities obtained in step 4 fixed. The codepthing misfit function plays the role of regularization ($\lambda_1 = 0, \lambda_2 \gg \mu > 0$).
6) Finally, we carry out differential semblance in angle optimization of PP and PS CIGs jointly to obtain estimates for the parameters v_{P0}, ε, and δ and keeping the v_{P0}/v_{S0} ratio obtained in steps 1–4 fixed. Again, the codepthing misfit function plays the role of regularization ($\lambda_1 = \lambda_2 \gg \mu > 0$).

The following subsections elaborate on these steps.

Step 1: Isotropic PP reflection tomography

The only parameter entering this step is the P-wave velocity, parameterized following Billette and Lambaré (1998) and Foss et al. (2004) as

$$v_P(\mathbf{x}) = \sum_k (v_{Pk} + g_k x_3) I_k(\mathbf{x}) + \sum_j a_j B_j(\mathbf{x}). \qquad (7)$$

Equation 7 shows a decomposition of the parameterization into a linear trend within each layer and a global B-spline representation. The linear trend is described by a vertical velocity gradient g_k, a constant v_{Pk}, and an indicator function I_k that is equal to one in layer k and zero outside. The second summation in equation 7 is a cubic B-spline expansion with 3D splines $B_j(\mathbf{x})$ and coefficients a_j. This summation captures any departures from the layer-based model. The indicator functions control the regions of rapid variation while the splines control the slow variations. The complete parameter vector is the collection of coefficients $\mathbf{m}_P = (\{v_{Pk}, g_k\}, \{a_j\})$.

The interface geometry implied by $\{I_k\}$ is updated automatically in the search procedure. From the initial PP image, interfaces/reflectors are picked (in depth) and are then map-demigrated along the NIP rays to compute zero-offset time horizons/reflections. For the current velocity model, these time horizons are map-migrated to generate the new interface geometry. In the gradient computation, the interface geometry is kept fixed. We assume that the relative change in geometry is less significant than the relative change in velocities. However, in the line search, the geometry is updated. Because the new interface geometry needs the new model and not the current one, a few iterations are needed to stabilize this procedure. The P-wave velocity optimization itself follows a stepwise approach. First, we optimize with respect to the parameters in the layer-based description of equation 7. Then we add the B-splines and optimize with respect to their coefficients to capture features of the velocity function not described by the layer-based model. The ray tracing is always carried out in a smooth model. For smoothing, we sample the layered part in the model representation and match these samples to a second B-spline representation.

Step 2: Isotropic PS reflection tomography

We keep the P-wave velocity (obtained in step 1) fixed and parameterize the S-wave velocity in a manner similar to that for equation 7. The linear trends are described by vertical velocity gradients h_k and constants v_{Sk}; the spline coefficients are denoted by b_j. The parameters are collected in $\mathbf{m}_S = (\{v_{Sk}, h_k\}, \{b_j\})$. The interface geometry $\{I_k\}$ is kept fixed and is given by the P-wave velocity-model representation. We carry

DOI:10.1190/1.2049350

out DSA optimization of PS CIGs and obtain an isotropic S-wave velocity model.

Step 3: Generating data for codepthing

We generate a PS image using the isotropic P- and S-wave velocity models obtained in steps 1 and 2. On this image, we find and trace key reflectors that we are able to recognize in and pair with the PP image. In practice, these form a subset of the interfaces already found in the estimation of the PP layer geometry. The paired key reflectors are map-demigrated, and SS traveltimes and slopes are computed using equation 4.

Step 4: Codepthing PP and PS images

We use the picked PP reflectors from the isotropic processing and update the isotropic S-wave velocity to obtain depth-consistent PP and PS key reflectors by minimizing equation 5. This is done with optimization where the data are the SS traveltimes and slopes obtained in step 3. The search is constrained to the range of the forward-scattering operators in isotropic velocity models. In the presence of anisotropy, the PS CIGs again exhibit residual moveout, which is corrected for in step 5.

Step 5: Initial anisotropic PS reflection tomography

Following a model of coarse-layer anisotropy, we use constant values for Thomsen's ε and δ parameters within the layers defined by the indicator functions. The constant values are denoted by ε_k and δ_k on the support of I_k. We collect the parameters in $\mathbf{m}_{\varepsilon,\delta} = (\{\varepsilon_k, \delta_k\})$. With a B-spline contribution we could capture departures from the assumption of coarse-layer anisotropy.

The residual moveout introduced in step 4 is reduced by an initial anisotropic PS reflection tomography. (In view of the limited range of PP reflection data, we note that the velocity-model anisotropy will be determined mostly from the available PS reflection data.) In the absence of information needed to resolve the δ parameter, we set $\delta = 0$. We keep the P-wave velocity model obtained in step 1 and the ratio of P- and S-wave velocities obtained in step 4 fixed and estimate ε_k. The outcome of the optimization provides a working parameter ε that yields focused, depth-consistent PP and PS images yet with an uncertainty in absolute depth (because $\delta = 0$).

Step 6: Anisotropic PP and PS reflection tomography

Based on reflection moveout analysis, estimating the δ parameter requires well logs, large-offset and wide-azimuth PP and PS data in three dimensions in the presence of reflectors with a range of dips (Grechka et al., 2002), or other information concerning the depths of reflectors, as discussed by Audebert et al. (2001). If well-log information is present, the true depth of the reflectors can be obtained where the wells penetrate them. The true depth of a reflector, in the absence of too strong lateral heterogeneity, is governed by v_{P0}, the vertical P-wave velocity, which can be obtained by matching the PP reflectors to well markers by map migration, similar to equation 5. This also gives an estimate of δ.

In the absence of well information, there is only the estimate of the P-wave velocity function obtained in step 1, denoted by $\hat{v}_P$. In the absence of too strong lateral heterogeneity, this P-wave velocity is approximately an interval NMO velocity (Thomsen, 1986):

$$\hat{v}_P \approx v_{P\mathrm{NMO}} = v_{P0}\sqrt{1+2\delta}. \tag{8}$$

Based on Grechka and Tsvankin (2002a, their equation 4), the S-wave velocity obtained in step 2, denoted here by $\hat{v}'_S$, is also approximately an interval NMO velocity:

$$\hat{v}'_S \approx v_{S\mathrm{NMO}} = v_{S0}\sqrt{1+2\sigma}, \quad \sigma \equiv \left(\frac{v_{P0}}{v_{S0}}\right)^2(\varepsilon-\delta). \tag{9}$$

The S-wave NMO velocity depends on the difference $\varepsilon - \delta$, which is scaled by the squared v_{P0}/v_{S0} ratio through the σ parameter. [We use the fact that $v_{PS\mathrm{NMO}}$ is directly related to $v_{S\mathrm{NMO}}$ and $v_{P\mathrm{NMO}}$ (Tsvankin and Thomsen, 1994)].

However, after the codepthing step 4, the estimate, denoted by $\hat{v}_S$, will differ from $v_{S\mathrm{NMO}}$. In fact, codepthing should yield an estimate for v_{P0}/v_{S0}. Since we only estimate $\hat{v}_S$ in this procedure and keep $\hat{v}_P$ fixed, we have, in the presence of anisotropy,

$$\frac{\hat{v}_P}{\hat{v}_S} = \frac{v_{P0}\sqrt{1+2\delta}}{\hat{v}_S} = \frac{v_{P0}}{v_{S0}}. \tag{10}$$

This gives

$$\hat{v}_S = v_{S0}\sqrt{1+2\delta} \tag{11}$$

after codepthing [see also Audebert et al. (2001)].

In the presence of anisotropy, the ratio of interval NMO velocities and the ratio of vertical velocities can be very different. In the absence of too strong lateral heterogeneity, the v_{P0}/v_{S0} ratio can be estimated from the ratio of vertical PP and SS times obtained from NMO analysis for PP and PS reflections and kept fixed. To maintain the depth consistency obtained after step 4 while allowing anisotropy, the ratio of the vertical-interval P- and S-wave velocities is kept fixed in the remaining processing steps.

In step 6, if large surface offsets (and hence subsurface scattering angles) are available and reflectors with multiple dips appear in the subsurface, the local parameter $\eta = (\varepsilon - \delta)/(1 + 2\delta)$ can be determined from annihilating the PP CIGs. We can then determine all parameters to describe a TI medium.

FIELD-DATA EXAMPLE

We tested our procedure on an ocean-bottom seismic line from data over the Norwegian sector of the North Sea. Out of necessity, we used a 2.5D formalism developed by Foss et al. (2005), considering 3D wave propagation in a 2D model where all calculations are done in a properly chosen plane. The data were subjected to standard processing such as static corrections, designature, and multiple removal (p-z summation and τ-p deconvolution).

For isotropic PP reflection tomography (step 2) we used a 2D version of the P-wave parameterization in equation 7. Thus, the B-splines are two dimensional and $\mathbf{x} = (x_1, x_3)$ in the following. The B-spline nodes are sampled every 250 m in the horizontal direction and every 100 m in depth. In the optimization, a relatively dense sampling in depth was deemed

necessary because of the observed rapid velocity increases. We penalize oscillatory behavior (in depth) by regularization. The image resulting from a simple 1D optimization is used to identify the layering of the velocity model. The time horizons of the interface geometry in equation 7 were found from map demigration as described in the previous sections. Fourteen time horizons were used in the subsequent velocity-estimation steps to control the interface geometry in equation 7. The starting values of constant velocity and velocity gradient within the layers were taken from a nearby well. The initial P-wave model and the corresponding PP image are given in Figures 5a and 6a.

To construct a well-behaved misfit function and guarantee a numerically stable computation of the gradient, we bandpass filtered the data between 3 and 15 Hz. (Note that in the imaging, we use the original data bandwidth.) Given the limited offset range in the data and the method of stabilizing the search, we observed that data beyond 15 Hz did not provide a significant contribution to the model update. The derivatives in angle inside the misfit function are tapered at small and large angles to remove truncation effects. We normalized the misfit function following Chauris and Noble (2001) to reduce the influence of erroneous amplitude calculations and noise in the data (this could have been circumvented by making the GRT of the data to CIGs unitary). The gradient contributions were tapered as we approached the boundaries of the model or in places with low ray coverage. Before calculating both the gradient and the misfit function, we smoothed the CIGs by a simple $\{\frac{1}{4}, \frac{1}{2}, \frac{1}{4}\}$ convolution filter in angle and depth. In addition, a 2D Fourier dip filter (in depth and angle) was applied to suppress imaging artifacts and noise. The filter was applied adaptively, passing events with decreasing moveout as we approached uniform gathers. These considerations were taken into account in all subsequent calculations.

Fourteen CIGs were computed every 250 m from 1250 m onward. Each CIG was sampled every 0.5° up to 45° incoming P-wave reflection angles. Figure 7 shows a sample CIG initially and after four and seven iterations in the optimization. The resulting P-wave velocity model and corresponding PP image are given in Figures 5b and 6b, respectively. The optimization for the B-spline coefficients was carried out in the final couple of iterations, but this showed little improvement in the misfit function. Notice in particular the movement of the interface geometry between the final P-wave velocity model in Figure 5b and the initial one (Figure 5a).

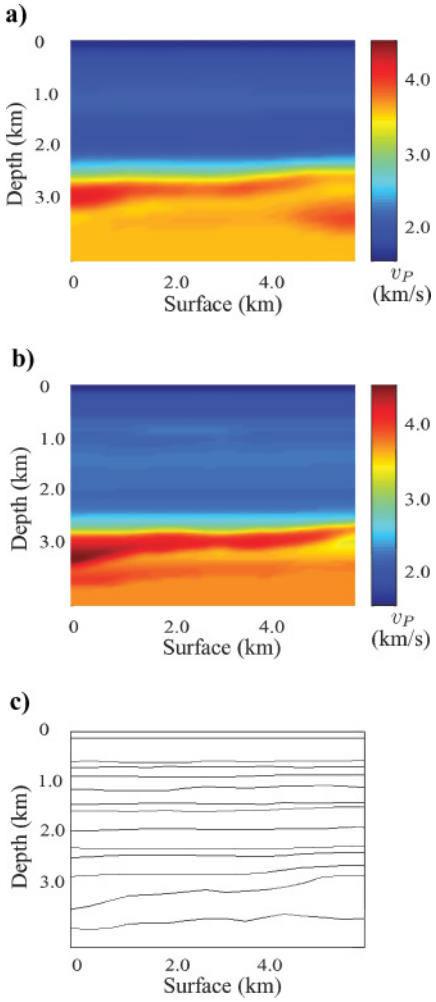

Figure 5. (a) Initial and (b) final P-wave velocity model from isotropic PP reflection tomography, with (c) the final interface geometry.

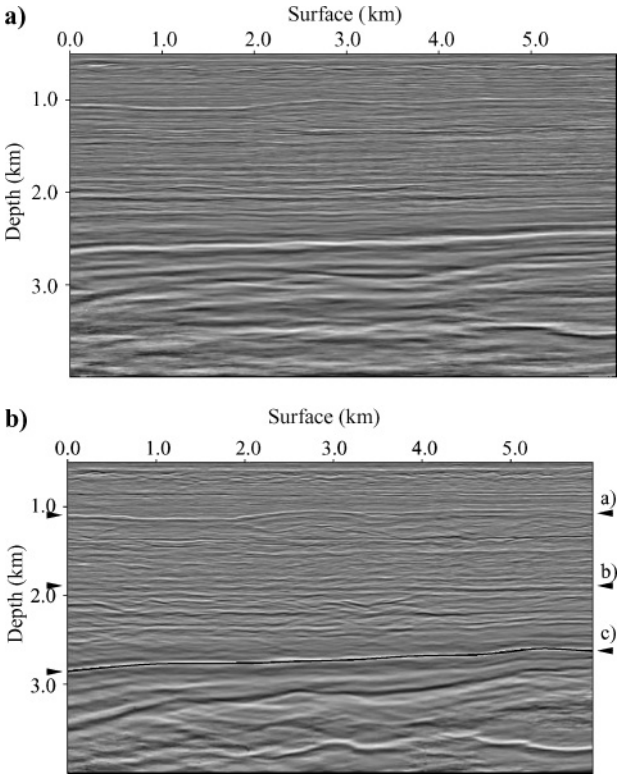

Figure 6. The PP image using (a) the initial isotropic P-wave velocity model in Figure 5a and (b) the final isotropic P-wave velocity model in Figure 5b. Arrows indicate a selection of interfaces of particular interest, denoted by a), b), and c).

Next, we carry out isotropic PS reflection tomography (step 2). The initial S-wave velocity model is chosen by a fixed v_S/v_P ratio for the entire model based on the final P-wave velocity (Figure 8a). The corresponding PS image is given in Figure 9a. The P-wave velocity model was considered reliable up to 45° incoming P-wave angle (the maximum angle used in the isotropic P-wave velocity analysis). We applied a tapered muting on the outgoing S-wave angles that, through Snell's law, are tied to incoming P-wave angles larger than 45°. We used eight positive and negative CIGs, $\mathcal{I}^+_{PS}$ and $\mathcal{I}^-_{PS}$, from surface position at 1750 m onward with a 300-m horizontal spacing. Figure 10 shows a sample CIG initially and after three and

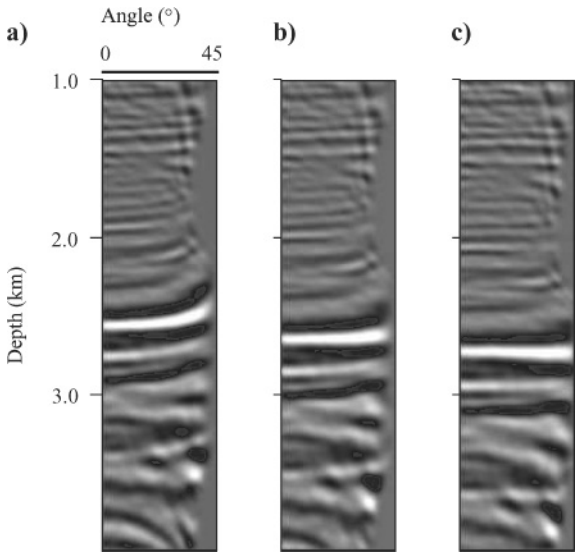

Figure 7. The PP CIG at 2.950 km of the isotropic P-wave velocity optimization after (a) zero, (b) four, and (c) seven iterations.

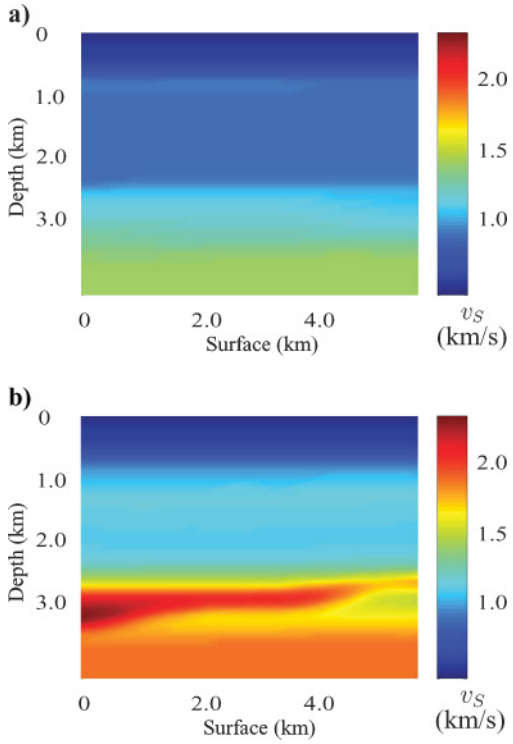

Figure 8. (a) Initial and (b) final S-wave velocity model obtained with isotropic PS reflection tomography.

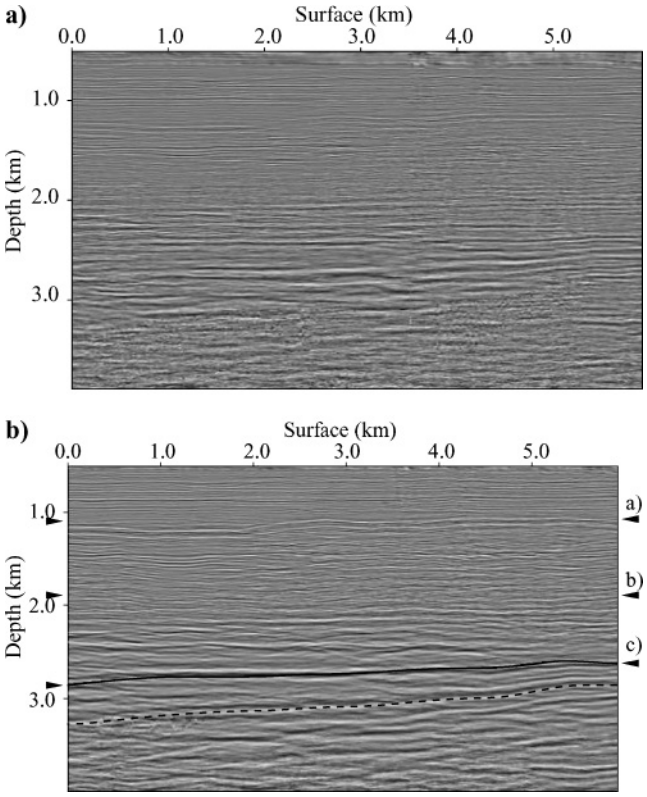

Figure 9. (a) The PS image using the initial S-wave velocity model in Figure 8a and using the P-wave velocity model in Figure 5b. (b) The PS image using the final S-wave velocity model in Figure 8b using the P-wave velocity model in Figure 5b. Arrows indicate the position of PP key reflections *a*, *b*, and *c*.

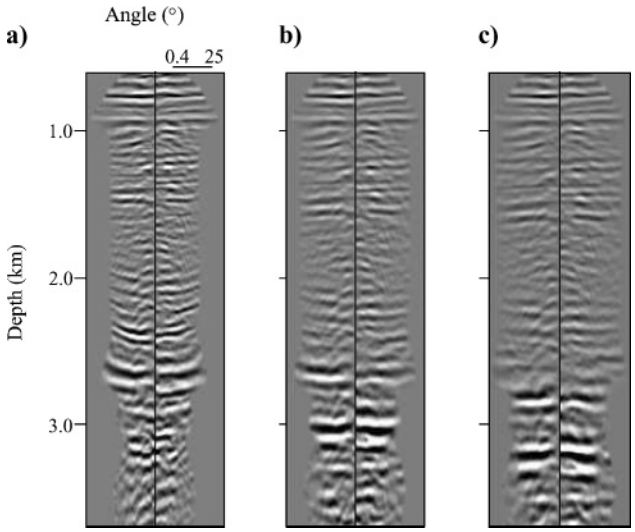

Figure 10. The PS CIG at 2.950 km of the isotropic S-wave velocity optimization after (a) zero, (b) two, and (c) five iterations.

five iterations in the optimization. The CIGs are displayed in pairs for the same horizontal position with the positive gather on the left and the negative gather on the right, as explained in Figure 1. They are plotted as functions of outgoing S-wave angle (contrary to convention), running from the indicated axis separating them in the positive and negative directions. The S-wave angle ranges from 0.4° to 25°.

The PS image resulting from the isotropic velocity analysis is given in Figure 9b. Superimposed are the arrows and tracing of the main reflector *c* as found on the PP image in Figure 6b. In the shallow part, reflector *a* of the PS image occurs slightly deeper than the corresponding reflector in the PP image (at the arrow). The depth discrepancy cannot be explained by the CIGs in Figure 10c, which are uniform and indicate a fitting model according to our DSA misfit measure. In the deeper parts, the superimposed PP reflector, *c* seems to match a PS reflector, but the geologically equivalent reflector on the PS image is indicated with the dotted line. Thus, under the isotropic assumption, the migrated, equivalent reflectors are several hundred meters apart in the PP and PS images.

To compute pure-mode SS traveltimes and slopes (step 3), we identify and pair several interfaces on both the PP and the PS images, which are then map-demigrated along the NIP rays to obtain the approximate SS traveltimes from equation 4. The key interfaces used are the three indicated with arrows in the PP image in Figure 9b.

The result of codepthing (step 4), yielding a depth-consistent PS image, is given in Figure 11 and is computed with the velocity model given in Figure 8b. The key reflectors in the PP and PS images are now at matching depths; but because of the isotropic assumption, the PS CIGs show residual moveout behavior again, as illustrated in Figure 12a. This concludes the isotropic processing procedure.

The initial anisotropic tomography (step 5) consists of estimating a working parameter ε. There is no information from wells intersecting the plane of consideration. In addition, the data are muted, so no large-offset data are available for PP reflections from the shallow part of the model. The optimization is carried out with $\delta = 0$, with a starting value $\varepsilon \equiv 0$ in the entire model. The PS CIGs are sampled every 350 m in the horizontal direction starting at 1750 m, still giving eight pairs of positive and negative CIGs.

The gradient in the optimization is tapered at 700 m (and above) and 2700 m (and below) based on ray coverage. All parameters except ε are kept fixed at their values obtained from isotropic velocity analysis. Figure 12 shows two sample PS CIGs. Sample 12a is the outcome of codepthing step 4. The shallow reflecting events are still quite uniform in these CIGs, but, as seen in Figure 11, they have in fact moved in the codepthing step. This means that the velocity update in step 4 is not detectable by the DSA misfit function because it stays in the range of the forward-scattering operator. The final PS CIG (Figure 12b) is optimized in two iterations. Most of the change applies to the middle depth interval, between 1500 and 2500 m. The resulting ε function and the corresponding image are given in Figures 13a and 14, respectively, where the indicators from the PP image (Figure 6b) are superimposed. The geologically equivalent reflectors on the PP and PS images now appear to match in depth. However, below reflector *c* in Figure 14 the PS image misses the structure clearly observable in the PP image. While investigating the PS CIG in Figure 12b in this region, we notice misalignment or alignment along lines with large angles. Since the formation of caustics is unlikely here, we attribute these to wave constituents violating our 2.5D single-scattering assumption (out-of-plane reflections or possibly multiples).

In Figure 15 we summarize the results by extracting a single trace, at 3200 m horizontal distance, from the images in Figures 6b (step 1), 9b (step 2), 11 (step 4), and 14 (step 5). One can clearly observe the mis-tie in depth between the first two traces, the shift in depth from the second to the third trace, and a reduction in oscillations from the third to the fourth trace. In Figure 16 we illustrate the change in the estimated v_{P0}/v_{S0} ratio as a result of codepthing. The change is significant where there is seismic illumination.

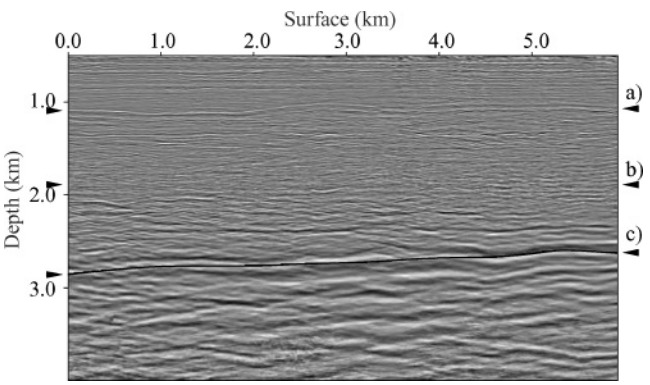

Figure 11. The PS image after codepthing. Arrows indicate the position of PP key reflectors *a*, *b*, and *c*.

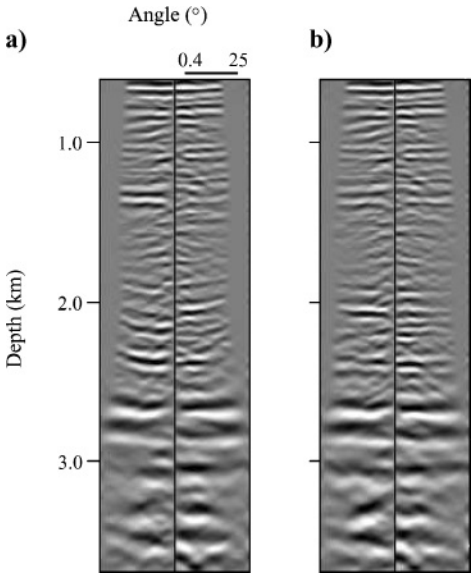

Figure 12. The PS CIG at 2.950 km of the initial ε optimization after (a) zero and (b) two iterations.

Depth fidelity

To examine how δ influences the results of the analysis carried out above, we consider joint PP and PS reflection tomography. In view of the limitations of the data acquisition in our case study, we have to depart from step 4. Because of offset (and hence angle) limitations, it is hard to obtain a reliable estimate for η from the PP CIGs. Instead of optimization, we scan the DSA function. We also scan a semblance function, energy normalized per CIG according to Chauris and Noble (2001). We investigate to what degree δ can be determined separately from ε, assuming a coarse-layer anisotropy model discussed earlier. For the scanning procedure we resort to a layer-stripping approach and limit the number of layers to five, as indicated in Figure 13b.

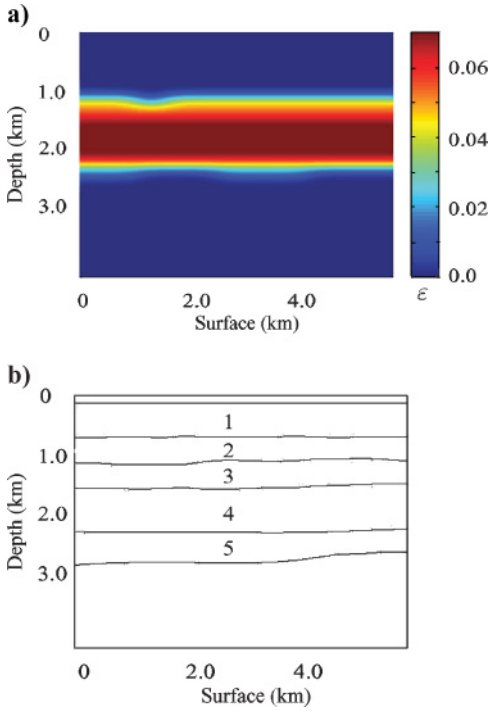

Figure 13. (a) The ε model after the initial anisotropic PS reflection tomography ($\delta = 0$) and (b) the five anisotropic layers used in the layer-stripping approach.

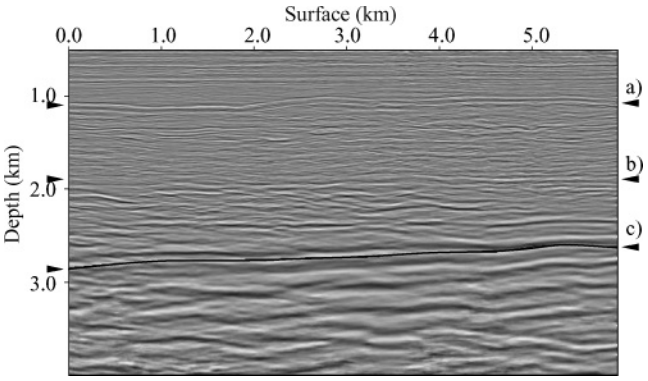

Figure 14. The PS image after initial anisotropic PS reflection tomography ($\delta = 0$). Arrows indicate the position of PP key reflectors *a*, *b*, and *c*.

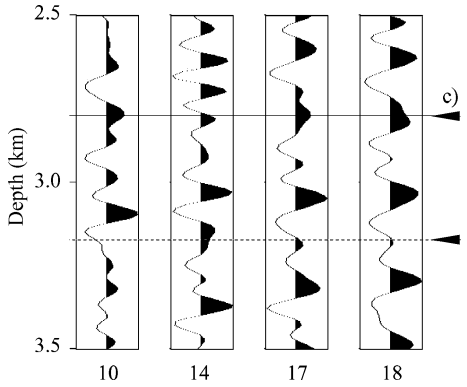

Figure 15. A single trace, at 3.200 km horizontal distance, from the images in Figures 6b (after isotropic PP reflection tomography), 9b (after isotropic PS reflection tomography), 11 (after codepthing), and 14 (after initial anisotropic PS reflection tomography); *c* is the deepest PP key reflector.

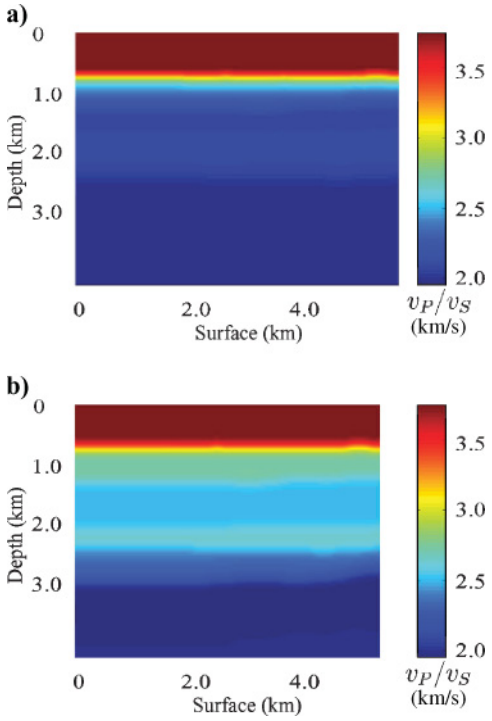

Figure 16. The $\hat{v}_P/\hat{v}_S$ ratios (a) before and (b) after codepthing.

The interfaces in this geometry form a subset of the set of interfaces in the geometry in Figure 5c. The top layer (water) and the bottom layer, below approximately 2700 m, are assumed to be isotropic. Isotropic parameters are taken from steps 1, 2, and 4; the sampling of CIGs is the same as in step 5.

Figure 17 illustrates the shapes of the misfit functions for the five different layers as functions of ε and δ. The general shapes of the DSA and semblance misfit functions are similar but not the same. In the layer-stripping approach, we use the optimal (ε, δ) values obtained in the layers above the layer in which the parameters are under investigation. Shown, by column, are the semblance misfits for PS, PP, their normalized sum, and our joint PP, PS DSA misfit function ($\lambda_1 = \lambda_2 = 1, \mu = 0$). The PP and PS semblance functions are plotted on the same scale. In the PS semblance plot, the apparent valley at a 45° angle is governed by $(\varepsilon - \delta)$ as in equation 9. This indicates the feasibility of detecting anisotropy in the PS CIGs without discriminating between the two parameters. In the PP semblance plot we are unable to observe significant change in the value of the misfit function with changing anisotropy, which can be attributed to the limited data offset range.

In the joint PP, PS semblance and the joint PP, PS DSA misfit plots, the lines

$$\varepsilon - \hat{\varepsilon} = \delta - \hat{\delta}, \tag{12}$$

are drawn, where $\hat{\varepsilon}$ and $\hat{\delta}$ are optimal values for ε and δ in each layer and can be found in Table 1. The vertical white lines in these plots indicate the $\hat{\delta}$ values. In the first three layers, the values are chosen using the PS semblance plot only, with $\delta = 0$, since there appears to be insufficient resolution in δ. In layers four and five we use the joint PP, PS semblance plots. In these layers we estimate values for ε and δ by locating the semblance misfit minimum after analyzing the joint PP, PS DSA misfit function first. In the deepest layer, a threshold on the DSA misfit function limits the region where the semblance misfit minimum is to be found and thus enables us to discriminate between the two apparent minima in the semblance misfit function. Most anisotropy appears in layer four, and layer five is weakly, elliptically anisotropic ($\eta = 0$). We emphasize that the values for ε and δ are for the application in processing only. In the calculations we used a fixed depth window of the CIGs. This implies, for example, that if δ becomes too negative, an event can move out of this depth window and hence no longer contribute to the misfit. A final PP CIG and corresponding PS CIG for the $\hat{\varepsilon}$ and $\hat{\delta}$ values in Table 1 are shown in Figure 18. The corresponding depth images are shown in Figure 19.

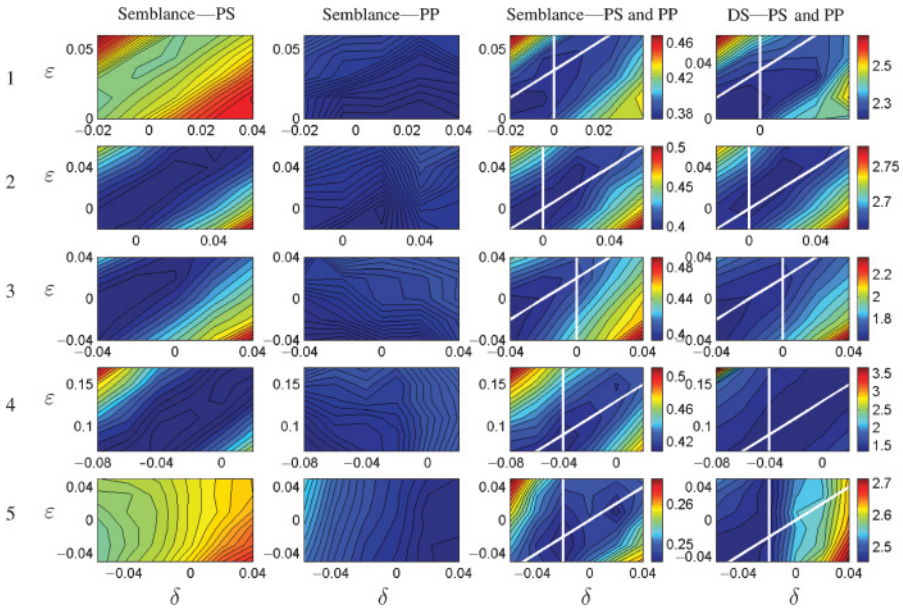

Figure 17. Contour plots for anisotropic layers 1–5 (vertical direction) and misfit plots for PS, PP, and PP + PS semblance and differential semblance in angle for PP + PS. (Here, one minus the normalized semblance is plotted as semblance, yielding a minimization problem.) The white vertical lines correspond with the δ values of Table 1.

Table 1. Anisotropic parameter values resulting from layer stripping.

Layer	$\hat{\varepsilon}$	$\hat{\delta}$
1	0.035	0.0
2	0.0	0.0
3	0.02	0.0
4	0.09	−0.04
5	−0.02	−0.02

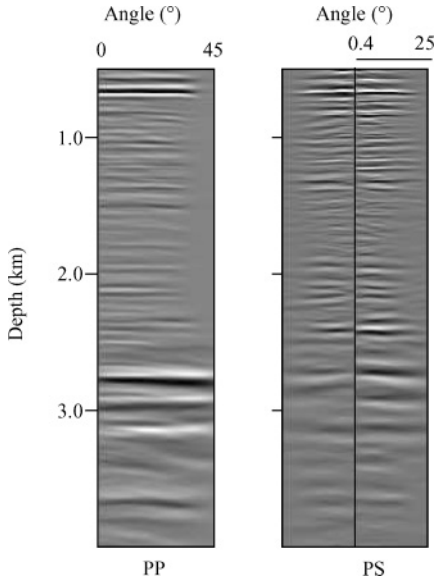

Figure 18. Final PP and PS CIGs at 2.950 km after anisotropic model update obtained following a scanning/layer-stripping approach. The gathers have been filtered in dip.

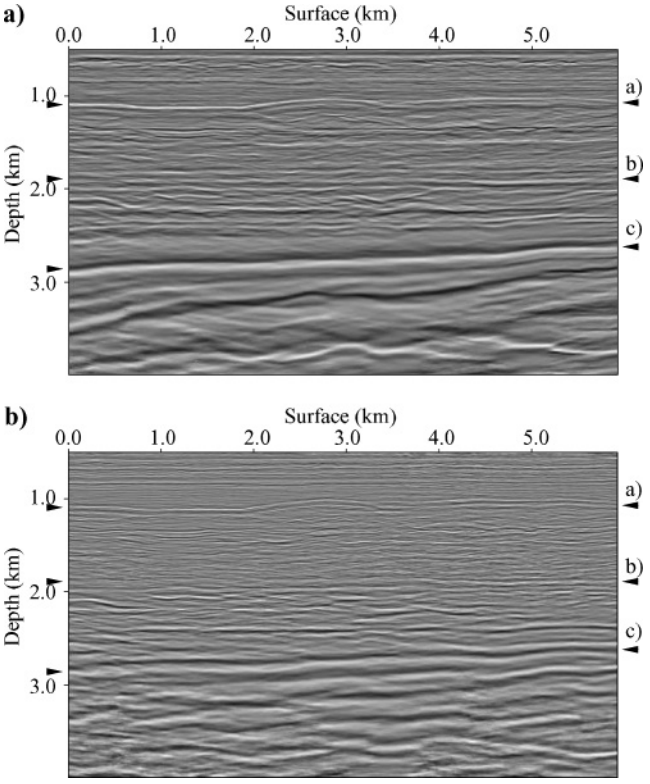

Figure 19. (a) PP and (b) PS images using the anisotropic parameters obtained from layer stripping. Arrows indicate the position of PP key reflectors *a*, *b*, and *c*.

DISCUSSION

We present a finite-frequency reflection tomographic approach to obtain depth-consistent PP and PS images by combining DSA and map migration/demigration, enabling automatic measurement of any mis-tie in depth. This approach involves an extension of DSA to converted waves as well as the development of a codepthing measure. The codepthing procedure is derived from the zero-scattering-angle case of Grechka and Tsvankin's PP + PS = SS concept. When the velocity model is far from the true model or when there is a significant inconsistency between the models governing the P-wave leg and the S-wave leg of the PS scattering event, the approximation we make in the PP + PS = SS concept deteriorates. Also, the current codepthing procedure, based on zero scattering angle, fails to apply in the presence of caustics. Then the codepthing procedure can be refined by using the PP + PS = SS approach to compute prestack SS traveltimes and slopes and incorporating finite-offset map (de)migration.

The tying of reflectors on PP and PS images forces us to consider anisotropy. This is observed by several authors, e.g., Audebert et al., 2001. Codepthing gives a compressional- and shear-wave velocity model based on a working TI medium (Thomsen's $\delta = 0$) assumption. We also try to estimate δ separately from ε, with limited success, in part of the model; in this estimation we use a semblance measure applied to the PP and PS CIGs. We attempted an ε, δ parameter estimation in a layer-stripping manner. As expected, the best resolved parameter combination from PS reflection tomography is $\varepsilon - \delta$. We restrict ourselves to models of coarse-layered TI anisotropy with constant ε and δ in each layer and known orientation of the symmetry axis.

Our method shows the potential to achieve depth consistency and uniform CIGs at the same time. It relies on the ability to identify, interpret, and pair interfaces on the PP and PS images. Success depends on whether PS images of sufficient quality can be generated. One can argue that the current field-data example could have been solved by a less sophisticated method, such as one based on the generalized Dix approach (Grechka and Tsvankin, 2002a). Our method, however, extends far beyond the cases where the generalized Dix equation applies.

Sometimes, ocean-bottom seismic technology is applied where PP imaging from streamer data seems to fail. This can often be attributed to the use of an essentially inaccurate velocity model. Our approach to MVA is robust under the formation of caustics and, hence, should aid in resolving complex velocity models from PP reflections (Stolk and de Hoop, 2002; Brandsberg-Dahl et al., 2003b).

One of the potential applications of reflection tomography is pore-pressure prediction (Sayers et al., 2003). Our method can also yield an improved estimate of the local v_P/v_S ratio in the overburden or in a reservoir if a coherent reflector exists below it. This could be important in lithology determination.

ACKNOWLEDGMENTS

We thank Statoil for the North Sea data set and Børge Arntsen for the data handling. In addition, we thank Anders Sollid (Statoil) for many helpful discussions. S.-K. F. thanks the URE project at the Norwegian University of Science and Technology for financial support.

APPENDIX A

MIGRATION TO UNIFORM-ANGLE CIGs

Dip, scattering angle, and azimuth

We consider migration of seismic data in a 3D heterogeneous anisotropic elastic medium. The geometry is shown in Figure A-1, where the image point is denoted by $\mathbf{y} = (y_1, y_2, y_3)$. Source positions in the acquisition manifold are

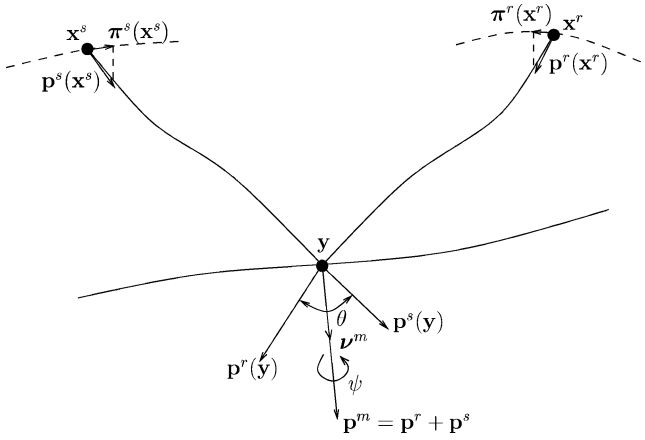

Figure A-1. Geometry of rays connecting the image point with the source and the receiver — an illustration of map (de)migration.

denoted by $\mathbf{x}^s$ and receiver positions by $\mathbf{x}^r$. The superscripts s and r indicate association with a ray from a source and a receiver, respectively. The slowness vector of the ray connecting the source point $\mathbf{x}^s$ with the image point $\mathbf{y}$ evaluated at the latter point is denoted by $\mathbf{p}^s(\mathbf{y})$; the value $\mathbf{p}^s(\mathbf{x}^s)$ indicates the slowness along this ray evaluated at the source. The projection $\boldsymbol{\pi}^s(\mathbf{x}^s)$ of $\mathbf{p}^s(\mathbf{x}^s)$ on the acquisition manifold is detected (via slope estimates) in the data. We furthermore introduce the phase direction $\boldsymbol{\alpha}^s = \mathbf{p}^s/|\mathbf{p}^s|$ and the phase velocity v^s according to $|\mathbf{p}^s| = 1/v^s$. A similar notation is used for the slowness vector-related quantities along the ray connecting the receiver with the image point, namely, $\mathbf{p}^r(\mathbf{y})$, $\mathbf{p}^r(\mathbf{x}^r)$, and $\boldsymbol{\pi}^r(\mathbf{x}^r)$, as well as $\boldsymbol{\alpha}^r$ and v^r. The polarization vector $\mathbf{h}$ is defined in the same manner as that for the slowness vector at the source, receiver, and image point. The migration dip $\boldsymbol{\nu}^m(\mathbf{y})$ is the direction $\boldsymbol{\nu}^m(\mathbf{y}) = \mathbf{p}^m(\mathbf{y})/|\mathbf{p}^m(\mathbf{y})|$ of the migration slowness vector $\mathbf{p}^m(\mathbf{y}) = \mathbf{p}^s(\mathbf{y}) + \mathbf{p}^r(\mathbf{y})$.

The scattering angle θ between incoming and scattered rays is defined by

$$\cos\theta = \boldsymbol{\alpha}^s \cdot \boldsymbol{\alpha}^r \quad \text{at } \mathbf{y}; \quad \theta = \theta(\mathbf{x}^r, \mathbf{y}, \mathbf{x}^s) \tag{A-1}$$

for a particular diffraction branch away from caustics at $\mathbf{x}^r$ or $\mathbf{x}^s$. The scattering azimuth ψ is the angular displacement of the vector

$$\boldsymbol{\psi}/|\boldsymbol{\psi}| \quad \text{with} \quad \boldsymbol{\psi} = (\boldsymbol{\alpha}^s \times \boldsymbol{\alpha}^r) \times \boldsymbol{\nu}^m \quad \text{at } \mathbf{y}; \qquad \psi = \psi(\mathbf{x}^r, \mathbf{y}, \mathbf{x}^s). \tag{A-2}$$

The two-way traveltime for a particular diffraction branch associated with a raypath connecting $\mathbf{x}^r$ with $\mathbf{x}^s$ via $\mathbf{y}$ is denoted by $T = T(\mathbf{x}^r, \mathbf{y}, \mathbf{x}^s)$.

Generalized Radon transform inversion

The medium is described by its stiffness tensor $c_{ijkl}(i, j, k, l \in \{1, \ldots, 3\})$ and density ρ. These parameters are decomposed as a sum of a smooth part [with superscript (0)] and a perturbation [with superscript (1)]:

$$\rho(\mathbf{x}) = \rho^{(0)}(\mathbf{x}) + \rho^{(1)}(\mathbf{x}), \quad c_{ijkl}(\mathbf{x}) = c^{(0)}_{ijkl}(\mathbf{x}) + c^{(1)}_{ijkl}(\mathbf{x}). \tag{A-3}$$

The estimation of the smooth part, the velocity model, is the objective of MVA, while the medium perturbations contain any singularities (reflectors) and are found by imaging inversion, given a velocity model. We assume now that the perturbations are jumps in the parameters across a smooth interface defined by the zero level set $\phi(\mathbf{x}) = 0$ of a function ϕ (de Hoop and Bleistein, 1997); multiple interfaces are treated with a finite collection of level-set functions. The interface normal is given by $\boldsymbol{\nu}_\phi = \nabla\phi/|\nabla\phi|$. Throughout, we use the subscript summation convention.

In preparing to migrate seismic data to uniform angle CIGs, we consider the following form of the generalized Radon transform (Sollid and Ursin, 2003):

$$\hat{S}_w(\mathbf{y}; \theta, \psi) = \int_{E_{\nu^m}} \partial_t \tilde{u}(\mathbf{x}^r, \mathbf{y}, \mathbf{x}^s)|\mathbf{p}^m(\mathbf{y})|^3 d\boldsymbol{\nu}^m, \tag{A-4}$$

in which $\mathbf{x}^s = \mathbf{x}^s(\mathbf{y}, \boldsymbol{\nu}^m, \theta, \psi)$ and $\mathbf{x}^r = \mathbf{x}^r(\mathbf{y}, \boldsymbol{\nu}^m, \theta, \psi)$, as illustrated in Figure A-1. This transform is a stripped-down version of the Brandsberg-Dahl et al. (2003a, their equation 20) inasmuch as the radiation-pattern inversion has been removed as well as the contribution $|\mathbf{p}^m(\mathbf{y})|/[\boldsymbol{\nu}^m(\mathbf{y}) \cdot \boldsymbol{\nu}_\phi(\mathbf{y})]$ to the obliquity factor. The domain of integration over $\boldsymbol{\nu}^m$ is indicated by $E^m_{\boldsymbol{\nu}} = E^m_{\boldsymbol{\nu}}(\theta, \psi) \subset S^2$ and reveals the illumination or acquisition footprint. The data corrected for amplitude, phase, and traveltime at a given image point are (Burridge et al., 1998, their equation 4.2)

$$\begin{aligned}\tilde{u}(\mathbf{x}^r, \mathbf{y}, \mathbf{x}^s) &= h^r_p(\mathbf{x}^r)\tilde{u}^{(1)}_{pq}[\mathbf{x}^r, T(\mathbf{x}^r, \mathbf{y}, \mathbf{x}^s), \mathbf{x}^s]h^s_q(\mathbf{x}^s) \\ &\times 2\left[\rho^{(0)}(\mathbf{x}^r)v^r(\mathbf{x}^r)v^r(\mathbf{y})v^s(\mathbf{y})\rho^{(0)}(\mathbf{x}^s)v^s(\mathbf{x}^s)\right]^{1/2} \\ &\times \left[\det \mathbf{Q}_2(\mathbf{x}^r, \mathbf{y}) \det \mathbf{Q}_2(\mathbf{y}, \mathbf{x}^s)\right]^{1/2},\end{aligned} \tag{A-5}$$

where $\rho^{(0)}$ denotes the bulk density of the smooth background while $\tilde{u}^{(1)}_{pq}$ denotes the multicomponent data corrected for a possible phase shift resulting from the presence of caustics:

$$\begin{aligned}\tilde{u}^{(1)}_{pq}[\mathbf{x}^r, T(\mathbf{x}^r, \mathbf{y}, \mathbf{x}^s), \mathbf{x}^s] &= \mathcal{H}^{\kappa(\mathbf{x}^r, \mathbf{y}, \mathbf{x}^s)} \\ &\times u^{(1)}_{pq}(\mathbf{x}^r, T(\mathbf{x}^r, \mathbf{y}, \mathbf{x}^s), \mathbf{x}^s).\end{aligned} \tag{A-6}$$

Here, $\mathcal{H}$ denotes the Hilbert transform ($\mathcal{H}^2 = -1$), while $\kappa(\mathbf{x}^r, \mathbf{y}, \mathbf{x}^s) = \kappa(\mathbf{x}^r, \mathbf{y}) + \kappa(\mathbf{y}, \mathbf{x}^s)$ is the accumulated KMAH index counting the number-phase changes because of caustics for the ray connecting $\mathbf{x}^r$ to the image point $\mathbf{y}$ and the ray connecting the image point $\mathbf{y}$ to $\mathbf{x}^s$. Furthermore, $\mathbf{Q}_2(\mathbf{x}^r, \mathbf{y})$ and $\mathbf{Q}_2(\mathbf{y}, \mathbf{x}^s)$ denote the relative geometric spreading (Červený, 2001) for the receiver and source rays, respectively. All factors that enter in equations A-4 and A-5 are calculated with the aid of kinematic and dynamic ray tracing.

Resolution analysis, assuming a band-limited signature common for all sources, then leads to the factorization

$$\hat{S}_w(\mathbf{y}; \theta, \psi) = \hat{S}^{(1)}(\mathbf{x}^\phi; \theta, \psi)w_{(\theta,\psi)}\left[p^\phi \boldsymbol{\nu}_\phi \cdot (\mathbf{y} - \mathbf{x}^\phi)\right], \quad \text{with} \quad |\mathbf{y} - \mathbf{x}^\phi| \text{ being small} \tag{A-7}$$

where

$$p^\phi = |\mathbf{p}^m(\mathbf{x}^\phi)| \quad \text{with} \quad \boldsymbol{\nu}^m(\mathbf{x}^\phi) = \boldsymbol{\nu}_\phi(\mathbf{x}^\phi), \tag{A-8}$$

which is the so-called "stretch factor" (Ursin, 2004).

AVA compensation

The relative contrast in the medium parameters is formally defined by the vector

$$\mathbf{c}^{(1)}(\mathbf{y}) = \left\{ \frac{\rho^{(1)}(\mathbf{y})}{\rho^{(0)}(\mathbf{y})}, \frac{c^{(1)}_{ijkl}(\mathbf{y})}{\rho^{(0)}(\mathbf{y})v^s_\circ(\mathbf{y})v^r_\circ(\mathbf{y})} \right\}^T. \tag{A-9}$$

Its dimension depends on the symmetry of the elastic medium. The PP and PS reflection problem in a VTI medium, which is treated in the field-data example, is of dimension five. We assume that $\mathbf{c}^{(1)}(\mathbf{y}) = \tilde{\mathbf{c}}^{(1)}[\mathbf{y}, \phi(\mathbf{y})]$, with $(\tilde{\mathbf{c}}^{(1)})'[\mathbf{y}, \phi(\mathbf{y})] = \mathbf{C}(\mathbf{y})\delta[\phi(\mathbf{y})]$, where $'$ denotes the derivative with respect to the second argument and $\mathbf{C}$ denotes the local magnitude of the jump across the zero level set of ϕ. Then (de Hoop and

Bleistein, 1997, their equation 38)

$$S^{(1)}(\mathbf{x}^\phi;\theta,\psi)=\mathbf{r}^T\left[\mathbf{x}^r\left(\mathbf{x}^\phi,\boldsymbol{\nu}_\phi,\theta,\psi\right),\mathbf{x}^\phi,\mathbf{x}^s\times\left(\mathbf{x}^\phi,\boldsymbol{\nu}_\phi,\theta,\psi\right)\right]\mathbf{C}(\mathbf{x}^\phi),\quad\text{(A-10)}$$

where $\mathbf{r}$ denotes the vector of radiation patterns

$$\mathbf{r}(\mathbf{x}^r,\mathbf{y},\mathbf{x}^s)=\left\{h^s_m(\mathbf{y})h^r_m(\mathbf{y}),\left[h^s_i(\mathbf{y})p^s_j(\mathbf{y})h^r_k(\mathbf{y})p^r_l(\mathbf{y})\right]\times v^s_\circ(\mathbf{y})v^r_\circ(\mathbf{y})\right\}^T.\quad\text{(A-11)}$$

Here, $v^s_\circ$ and $v^r_\circ$ are the phase velocities at $\mathbf{y}$ averaged over phase angles. We refer to $S^{(1)}$ as linearized scattering coefficients; $\hat{S}^{(1)}$ is a filtered realization of $S^{(1)}$, where the filter is determined by the illumination.

For the estimation of the smoothly varying parameters of the background medium (MVA), we use a slight modification of transform equation A-4, with

$$\mathcal{I}(\mathbf{y};\theta,\psi)=\int_{E_{\nu^m}}\partial_t\tilde{u}(\mathbf{x}^r,\mathbf{y},\mathbf{x}^s)\frac{|\mathbf{p}^m(\mathbf{y})|^3}{|\mathbf{r}(\mathbf{x}^r,\mathbf{y},\mathbf{x}^s)|}d\boldsymbol{\nu}^m,\quad\text{(A-12)}$$

replacing $\hat{S}_w(\mathbf{y};\theta,\psi)$. Here, $|\mathbf{r}(\mathbf{x}^r,\mathbf{y},\mathbf{x}^s)|$ is the Euclidean norm of the vector of radiation patterns. At specular reflection points, $S^{(1)}$ in equation A-10 is replaced by, $\mathbf{e}(\mathbf{x}^\phi;\theta,\psi)^T\mathbf{C}(\mathbf{x}^\phi)$, with $\mathbf{e}(\mathbf{x}^\phi;\theta,\psi)=\mathbf{r}[\mathbf{x}^r(\mathbf{x}^\phi,\boldsymbol{\nu}_\phi,\theta,\psi),\mathbf{x}^\phi,\mathbf{x}^s(\mathbf{x}^\phi,\boldsymbol{\nu}_\phi,\theta,\psi)]/|\mathbf{r}[\mathbf{x}^r(\mathbf{x}^\phi,\boldsymbol{\nu}_\phi,\theta,\psi),\mathbf{x}^\phi,\mathbf{x}^s(\mathbf{x}^\phi,\boldsymbol{\nu}_\phi,\theta,\psi)]|$. We anticipate that $\mathbf{e}$ is only weakly dependent on (θ,ψ); hence, Ursin (2004) refers to equation A-12 as amplitude-compensated migration.

For interpretation and comparisons, we use the structural image

$$\mathcal{I}(\mathbf{y})=\iint\mathcal{I}(\mathbf{y};\theta,\psi)\,d\theta d\psi.\quad\text{(A-13)}$$

Subscripts indicate whether a current CIG (equation A-12) or a structural image (equation A-13) is computed from PP or PS reflections: $\mathcal{I}_{PP}$ and $\mathcal{I}_{PS}$, respectively.

In the presence of caustics, $\mathcal{I}(\mathbf{y};\theta,\psi)$ as defined in equation A-12 commonly generates artifacts. A remedy for this is the use of the downward-continuation approach from which an angle transform can be extracted that generates CIGs in angle without artifacts (Stolk and de Hoop, 2004).

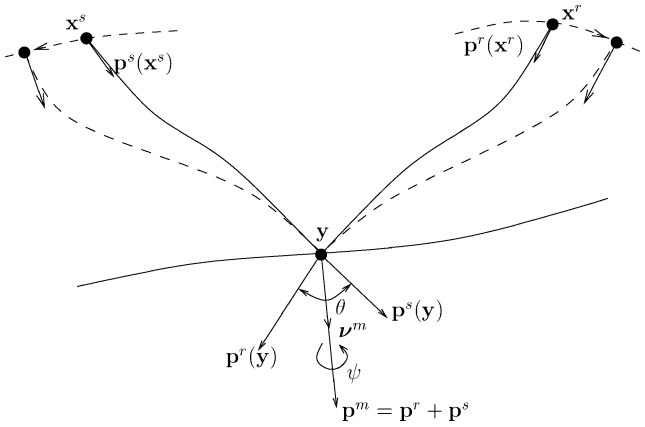

Figure A-2. The differential semblance misfit function in angle is differentiated, keeping the image point, scattering angle, azimuth, and migration dip fixed. Dashed lines indicate perturbed rays.

Map (de)migration

Map migration describes how the geometry of a reflection is mapped on the geometry of a reflector,

$$\Sigma:(\mathbf{x}^s,\mathbf{x}^r,t,\boldsymbol{\pi}^s,\boldsymbol{\pi}^r)\mapsto(\mathbf{y},\mathbf{p}^m)\quad\text{at}\quad t=T(\mathbf{x}^r,\mathbf{y},\mathbf{x}^s),\quad\text{(A-14)}$$

such that the normal to the reflector is given by $\boldsymbol{\nu}^m$. For a given value of (θ,ψ), this process can be reversed to yield map demigration:

$$\Omega\ :\ (\mathbf{y},\mathbf{p}^m,\theta,\psi)\mapsto[\mathbf{x}^s,\mathbf{x}^r,T(\mathbf{x}^r,\mathbf{y},\mathbf{x}^s),\boldsymbol{\pi}^s,\boldsymbol{\pi}^r].\quad\text{(A-15)}$$

Map demigration corresponding to the exploding reflector model is obtained by setting $\theta=0$. For pure-mode events, the receivers (at zero offset, $\mathbf{x}^r=\mathbf{x}^s$) are connected with the reflectors via NIP rays (Hubral and Krey, 1980).

Ray perturbation and optimization

In setting up the optimization in the main text, one must decide which quantities are kept fixed under perturbation of the velocity model between the reflector and the acquisition manifold: $(\mathbf{y},\mathbf{p}^m,\theta,\psi)$ or $(\mathbf{x}^s,\mathbf{x}^r,t,\boldsymbol{\pi}^s,\boldsymbol{\pi}^r)$. For DSA optimization, derived from the GRT, we keep the first set of variables fixed and differentiate the misfit functions $\mathcal{E}_{PP}$ and $\mathcal{E}_{PS}$ accordingly. A perturbation of the velocity model thus implies a perturbation of mapping Ω (Figure A-2). The derivative of the CIGs with the medium parameters can be evaluated with the aid of ray perturbation theory and can be found in Brandsberg-Dahl et al. (2003b, their equation 12).

In setting up the optimization for codepthing, based on equation 5 in the main text, one must decide again which quantities are kept fixed under perturbation of the velocity model between the reflector and the acquisition manifold. We keep the input variables to Σ fixed; hence, a perturbation of the velocity model implies a perturbation of mapping Σ.

It seems that we introduce an ambiguity: The continuation of the GRT with velocity is based on keeping the input variables to map demigration (Ω in equation A-15) fixed, while the continuation of the codepthing is based on keeping the input variables to map migration (Σ in equation A-14) fixed. The flow of the image points with changing velocity model (Iversen, 2001) coincides with loosely called "velocity rays" (Fomel, 1997). Since the full misfit function is a superposition of constituent misfit functions revealing the different steps, the ambiguity is allowed.

REFERENCES

Alerini, M., S. Le Bégat, G. Lambaré, and R. Baina, 2002, 2D PP- and PS-stereotomography for a multicomponent data set: 72nd Annual International Meeting, SEG, Expanded Abstracts, 838–841.

Alkhalifah, T., and I. Tsvankin, 1995, Velocity analysis for transversely isotropic media: Geophysics, **60**, 1550–1566.

Al-Yahya, K., 1989, Velocity analysis by iterative profile migration: Geophysics, **54**, 718–729.

Audebert, F., P.-Y. Granger, C. Gerea, and A. Herrenschmidt, 2001, Can joint PP and PS velocity analysis manage to corner δ, the anisotropic depthing parameter?: 71st Annual International Meeting, SEG, Expanded Abstracts, 145–148.

Berthet, P., Y. Le Stunff, P. Guillaume, J. Mispel, and J. Boelle, 2001, PP and PS travel time anisotropic tomography on case study: 63rd Annual Conference, European Association of Geophysicists and Engineers, Extended Abstracts.

Billette, F., and G. Lambaré, 1998, Velocity macro-model estimation from seismic reflection data by stereotomography: Geophysical Journal International, **135**, 671–690.
Brandsberg-Dahl, S., M. V. de Hoop, and B. Ursin, 2003a, Focusing in dip and AVA compensation on scattering-angle/azimuth gathers: Geophysics, **68**, 232–254.
———, 2003b, Seismic velocity analysis in the scattering-angle/azimuth domain: Geophysical Prospecting, **51**, 295–314.
Broto, K., A. Ehinger, J. H. Kommedal, and P. G. Folstad, 2003, Anisotropic traveltime tomography for depth consistent imaging of PP and PS data: The Leading Edge, **22**, 114–119.
Bube, K. P., 1995, Uniqueness of reflector depths and characterization of the slowness null space in linearized seismic reflection tomography: SIAM Journal on Applied Mathematics, **55**, 255–266.
Bube, K. P., and M. A. Meadows, 1999, The null space of a generally anisotropic medium in linearized surface reflection tomography: Geophysical Journal International, **139**, 9–50.
Burridge, R., M. V. de Hoop, D. Miller, and C. Spencer, 1998, Multiparameter inversion in anisotropic media: Geophysical Journal International, **134**, 757–777.
Červený, V., 2001, Seismic ray theory: Cambridge University Press.
Chauris, H., and M. Noble, 2001, Two-dimensional velocity macro model estimation from seismic reflection data by local differential semblance optimization: Application to synthetic and real data sets: Geophysical Journal International, **144**, 14–26.
de Hoop, M. V., and N. Bleistein, 1997, Generalized Radon transform inversions for reflectivity in anisotropic elastic media: Inverse Problems, **13**, 669–690.
Fomel, S., 1997, Velocity continuation and the anatomy of residual prestack migration: 67th Annual International Meeting, SEG, Expanded Abstracts, 1762–1765.
Foss, S.-K., M. V. de Hoop, and B. Ursin, 2005, Linearized 2.5-D parameter imaging-inversion in anisotropic elasic media: Geophysical Journal International, doi:10.1111/j.1365–246X.2005.02599.x.
Foss, S.-K., B. Ursin, and A. Sollid, 2004, A practical approach to automated PP angle tomography: Geophysical Prospecting, **52**, 663–669.
Gjoystdal, H., and B. Ursin, 1981, Inversion of reflection times in three dimensions: Geophysics, **46**, 972–983.
Grechka, V., and I. Tsvankin, 2002a, The joint nonhyperbolic moveout inversion of PP and PS data in VTI media: Geophysics, **67**, 1929–1932.
———, 2002b, PP + PS = SS: Geophysics, **67**, 1961–1971.
Grechka, V., A. Pech, and I. Tsvankin, 2002, Multicomponent stacking-velocity tomography for transversely isotropic media: Geophysics, **67**, 1564–1574.
Herrenschmidt, A., P.-Y. Granger, F. Audebert, C. Gerea, G. Etienne, A. Stopin, M. Alerini, et al., 2001, Comparison of different strategies for velocity model building and imaging of PP and PS real data: The Leading Edge, **20**, 984–995.
Hubral, P., and T. Krey, 1980, Interval velocities from seismic reflection time measurements: SEG.
Iversen, E., 2001, First-order perturbation theory for seismic isochrones: Studia Geophysica et Geodaetica, **45**, 394–444.
Kleyn, A. H., 1977, On the migration of reflection-time contour maps: Geophysical Prospecting, **25**, 125–140.
Plessix, R.-E., F. ten Kroode, and W. Mulder, 2000, Automatic cross-well tomography by differential semblance optimization: Theory and gradient computation: Geophysical Prospecting, **48**, 913–935.
Sayers, C. M., T. J. H. Smit, C. van Eden, R. Wervelman, B. Bachmann, T. Fitts, J. Bingham et al., 2003, Use of reflection tomography to predict pore pressure in overpressured reservoir sands: 73rd Annual International Meeting, SEG, Expanded Abstracts, 1362–1365.
Sollid, A., and N. Ettrich, 1999, Coherency optimization of tranversely isotropic velocity models via PP/PS prestack migration: 69th Annual International Meeting, SEG, Expanded Abstracts, 1707–1710.
Sollid, A., and B. Ursin, 2003, Scattering-angle migration of OBS data in weakly anisotropic media: Geophysics, **68**, 641–655.
Stolk, C. C., and M. V. de Hoop, 2002, Microlocal analysis of seismic inverse scattering in anisotropic elastic media: Communications in Pure and Applied Mathematics, **55**, 261–301.
———, 2004, Seismic inverse scattering in the downward continuation approach: http://www.cwp.mines.edu/reports_list.html.
Stopin, A., and A. Ehinger, 2001, Joint PP PS tomographic inversion of the mahogany 2D–4-C OBC seismic data: 71st Annual International Meeting, SEG, Expanded Abstracts, 837–840.
Stork, C., and R. W. Clayton, 1986, Analysis of the resolution between ambiguous velocity and reflector position for traveltime tomography: 56th Annual International Meeting, SEG, Proceedings, 545–550.
Symes, W., 2000, Asymptotic analysis of differential semblance for layered acoustics: http://www.caam.rice.edu.
Symes, W., and J. Carazzone, 1991, Velocity inversion by differential semblance optimization: Geophysics, **56**, 654–663.
Taner, M. T., and F. Koehler, 1969, Velocity spectra — Digital computer derivation and applications of velocity functions: Geophysics, **34**, 859–881.
Thomsen, L., 1986, Weak elastic anisotropy: Geophysics, **51**, 1954–1966.
———, 1999, Converted-wave reflection seismology over inhomogeneous, anisotropic media: Geophysics, **64**, 678–690.
Tsvankin, I., and L. Thomsen, 1994, Nonhyperbolic reflection moveout in anisotropic media: Geophysics, **59**, 1290–1304.
Ursin, B., 2004, Parameter inversion and angle migration in anisotropic elastic media: Geophysics, **69**, 1125–1142.
Versteeg, R. J., 1993, Sensitivity of prestack depth migration to the velocity model: Geophysics, **58**, 873–882.
Whitcombe, D. N., 1994, Fast model building using demigration and single-step ray migration: Geophysics, **59**, 439–449.